RSC Advances

ROYAL SOCIETY OF CHEMISTRY

www.rsc.org/advances

RSC Advances

ARTICLE

Luminescence and structural analysis of Ce^{3+}, Er^{3+} doped and Ce^{3+}-Er^{3+} codoped $Ca_3Sc_2Si_3O_{12}$ garnets: Influence of the doping concentration in the energy transfer processes.

R. Fernández-González[a,c], J.J. Velázquez*[a,b,d], V.D. Rodríguez[b,c], F. Rivera-López[e], A. Lukowiak[f], A. Chiasera[g], M. Ferrari[g], R.R. Gonçalves[h], J. Marrero-Jerez[a,c], F. Lahoz[b,i] and P. Núñez[a,c]

We present a research on $Ca_3Sc_2Si_3O_{12}$ garnets doped with Ce^{3+} and Er^{3+} ions that were synthesized by the freeze-drying precursor method. The structural characterization was performed by X-ray diffraction (XRD) and X-ray photoelectron spectroscopy (XPS). Scanning Electron Microscopy (SEM) images of the calcined material were studied. Nanocrystals of $Ca_3Sc_2Si_3O_{12}$ where obtained by calcining the precursor at 1200 ºC for 4 h with a mean size about 100 nm. The luminescence features of Ce^{3+} and Er^{3+} doped samples indicated that these ions are effectively incorporated into the crystalline phase. In addition, the codoping with Ce^{3+}-Er^{3+} ions results in energy transfer processes from Ce^{3+} to Er^{3+} ions which let to enhance the Near-Infrared luminescence at 1.5 µm. The efficiency of these non-radiative energy transfer process has been studied by means of excited state dynamics as a function of the doping concentration. From these results we have found that Near-Infrared Er^{3+} luminescence efficiency under VIS Ce^{3+} excitation is maxima for $1Ce^{3+}$-$1Er^{3+}$ codoped $Ca_3Sc_2Si_3O_{12}$ garnets (in mol%). Luminescence quenching for higher Er^{3+} ions concentration is observed.

Received 00th January 20xx,
Accepted 00th January 20xx
DOI: 10.1039/x0xx00000x
www.rsc.org/

1. Introduction

Rare earth (RE) doped luminescent materials have attracted much attention due to their potential applications in optoelectronic technology. In particular, Er^{3+} doped materials could be helpful in germanium based photovoltaic systems to make better use of the solar spectrum. They could enhance the photon obtaining in the near infrared (NIR) where the germanium cells shows the highest conversion efficiency. The down-conversion involved processes are based on energy transfer mechanism between RE pairs, starting with sensitizers that have strong absorption in the UV-blue region[1,2].

One of the most promising candidates to be used as sensitizer is Ce^{3+} ion. The absorption of Ce^{3+} is originated from the allowed electric-dipole transition from the 4f ground state to the 5d excited one, resulting in a high absorption cross section in the UV-blue spectral region[3]. This absorption can be tuned by selection of the host material due to the strong dependence of the Ce^{3+} ion level diagram on the crystalline field, which also takes to appreciable shifts on luminescence band[4,5]. On the other hand, with respect to the typical option of Yb^{3+} ions like luminescent center after energy transfer from Ce^{3+} 5d level[6], Er^{3+} ions are an excellent option for energy conveyance from UV to NIR photons at 1550 nm, because they could involve the obtaining of three NIR photons after absorption of UV-blue photons[7], with a potential effective quantum efficiency close to 300%. The use of Ce^{3+} ions as sensitizers enhances the absorption in the UV-blue, where Er^{3+} ions only present relatively weak and narrow absorption peaks.

The combination of Ce^{3+} and Er^{3+} ions with the suitable host would optimize the conversion of UV-VIS radiation into NIR. In this sense, nano-garnets with the general formula $A_3B_2C_3O_{12}$ have been widely studied after doping with RE ions due to their potential applications in optoelectronics. In particular, silicate garnet with the composition $Ca_3Sc_2Si_3O_{12}$ (CSSO) has been synthesized by different as solid-state reaction, microwaves or sol-gel. Moreover their luminescence properties have been studied after doping doping with several lanthanides (Ce^{3+}, Tb^{3+}, Pr^{3+}, Eu^{3+} or Nd^{3+})[8-15]. But, as far as we know, they have not been studied after codoping with Ce^{3+} and Er^{3+}.

[a] Departamento de Química, U.D. Química Inorgánica, Universidad de La Laguna, 38206 La Laguna, Tenerife, Spain.
[b] Departamento de Física, Universidad de La Laguna, 38206 La Laguna, Tenerife, Spain.
[c] Institute of Materials and Nanotechnology, Universidad de La Laguna, 38206 La Laguna, Tenerife, Spain.
[d] Instituto de Cerámica y Vidrio (CSIC), C/Kelsen 5, 28049 Madrid, Spain.
[e] Sistema Multitécnicas de Análisis de Superficies. Servicio General de Apoyo a la Investigación (SEGAI), Universidad de La Laguna, 38206, La Laguna, Tenerife, Spain.
[f] Institute of Low Temperature and Structure Research PAS, 50-422 Wroclaw, Poland.
[g] IFN–CNR CSMFO Lab., and FBK Photonics Unit, I-38123 Trento, Italy.
[h] Departamento de Química, Faculdade de Filosofia, Ciências e Letras de Ribeirão Preto, Universidade de São Paulo-Av. Bandeirantes, 3900, CEP 14040-901, Ribeirão Preto/SP, Brazil.
[i] Instituto Universitario de Estudios Avanzados en Atómica, Molecular y Fotónica (IUdEA), Universidad de La Laguna, 38206, La Laguna, Tenerife, Spain.

In this work, Ce^{3+} and Er^{3+} single- and codoped $Ca_3Sc_2Si_3O_{12}$ garnets have been synthesized by using a freeze-drying precursor route. Structural characterization by XRD and SEM techniques were performed to confirm the crystal structure of CSSO garnet and to observe the microstructure of the sintered samples. Cerium ions could be present in the samples as Ce^{4+} ions, which are not luminescent. By this reason XPS was used for estimating the relative concentration of the two oxidation states of Ce (III and IV) in the surface of the samples. Finally, photoluminescent properties of single doped and codoped garnets and excite state dynamics in codoped samples have been studied in order to analyze the efficiency of the energy transfer mechanisms.

2. Experimental

2.1 Synthesis

Undoped and Ce^{3+}-Er^{3+} single- and co-doped $Ca_3Sc_2Si_3O_{12}$ polycrystalline powders were synthesized by the freeze-drying precursor method [16-18], using $CaCO_3$ (99%, Merck), Sc_2O_3 (99.9%, Aldrich), Tetraethyl orthosilicate ($C_8H_{20}O_4Si$) (98%, Aldrich), $Ce(NO_3)_3{\cdot}6H_2O$ (99.99%, Aldrich) and $Er(NO_3)_3{\cdot}5H_2O$ (99.9%, Aldrich) as reagents. Table 1 presents the different dopant concentrations that have been considered in this work. Hydrated metal nitrates were previously studied by thermogravimetric analysis to determine the cation content. Stoichiometric quantities of the reagents were individually dissolved in distilled water and then mixed together. Afterwards, ethylenediaminetetraacetic acid (EDTA) (99.7% Aldrich) was added as complexing agent, in 1:1 ligand to metal molar ratio, to prevent precipitation.

The pH of the solution, which was initially acid, was adjusted around 7-8 by adding aqueous ammonia. Drops of the as-obtained solution were subsequently flash-frozen by pouring them into liquid nitrogen. In this way, each frozen drop retains the homogeneous cation distribution of the original solution. Then, the sample is freeze-dried in a HetoLyolab 3000 (Heto-Holten A/S) freeze-dryer equipment for 3 days. The obtained highly hygroscopic amorphous precursor was immediately pre-calcined at 400 ºC for 2 hours to prevent rehydration and to eliminate the organic matter. Finally, the dry powders were pressed at 10 Tm in a hydrostatic press in order to obtain pellets which were calcined in alumina crucibles at 1200 ºC during 4 hours.

Sample	Ce^{3+}	Er^{3+}
CSSO	0	0
CSSO-1Ce	1	0
CSSO-4Ce	4	0
CSSO-0.5Er	0	0.5
CSSO-1Er	0	1
CSSO-1Ce0.5Er	1	0.5
CSSO-1Ce1Er	1	1
CSSO-1Ce2Er	1	2
CSSO-1Ce4Er	1	4

Table 1. Samples codes and dopant content, in mol%, in the $Ca_3Sc_2Si_3O_1$ (CSSO) garnets studied in this work.

2.2 Experimental Setup

X-ray analysis (XRD) were carried out by using a Philips difractometer equipped with an X'Celerator detector and a Cu anode (Cu $K\alpha_1,\alpha_2$) in the 20-80 2θ diffraction range. The microstructure of the samples was studied by scanning electron microscopy (SEM) (Jeol LTD, mod. JSM-6300). All samples were covered with a thin film of silver to avoid charging problems and to obtain better image definition. The high-resolution X-ray photoelectron spectroscopy (XPS) spectrum was collected on an ESCALAB 250 spectrometer, using a monochromatized Al K_α X-ray radiation (hv=1486.6 eV) with a spot size of 650 µm. The spectrometer energy calibration was performed using the Au $^4f_{7/2}$ and Cu $^2p_{3/2}$ photoelectron lines. The chemical shifts in the spectra were corrected with reference to the binding energy of the C 1s core level spectrum, corresponding to the carbon contamination layer at 284.6 eV. This peak arises from a minor quantity of contaminants and is generally accepted to be independent of the chemical state of the sample under investigation. The spectrum was collected in constant analyzer energy (CAE) mode, with pass energy of 20 eV and with an energy resolution of about 0.1 eV. For all the measurements, pressure in the ultra-high vacuum analysis chamber was lower than $8x10^{-9}$ mbar, avoiding that the ejected photoelectron interact with gas molecules. Laser Raman spectra were recorded on a Jobin Yvon/Labram HR spectrometer using a 632.8 nm excitation of a He–Ne laser. Double beam Shimadzu UV-2450 Scan UV–Visible spectrophotometer was used to record the reflectance spectra over a wavelength range of 200–800 nm. Emission and excitation spectra were recorded by using a 300 W Xenon lamp with a double-grating monochromator (SPEX 1680). These spectra were collected by using a spectrometer (ANDOR Shamrock) equipped with an UV-VIS-NIR CCD camera (Newton CCD) and a NIR InGaAs or a single-grating monochromator (SPEX 1681) equipped with a photomultiplier tube (Hamamatsu R928). The spectral response of the set-up was taken into account. The luminescence decays in the nanosecond scale were measured by using a LifeSpec II spectrometer of Edinburgh Instruments. The samples were excited by 70 ps pulses with 1MHz repetition rate produced by a semiconductor laser operating at 405 nm. A multi-channel plate photomultiplier tube was used for the detection. The system was operated in time correlated single photon counting mode and had an instrumental response function (IRF) with a half maximum width of about 70 ps. The millisecond kinetics of luminescence were recorded by using an optical parametrical oscillator (OPO) pumped by the 3rd harmonic of a YAG:Nd laser as the excitation source. The signal was detected with a digital storage oscilloscope controlled by a personal computer. The samples were excited by 6 ns pulses with 20 Hz repetition rate. The time resolution of this setup was 20 ns.

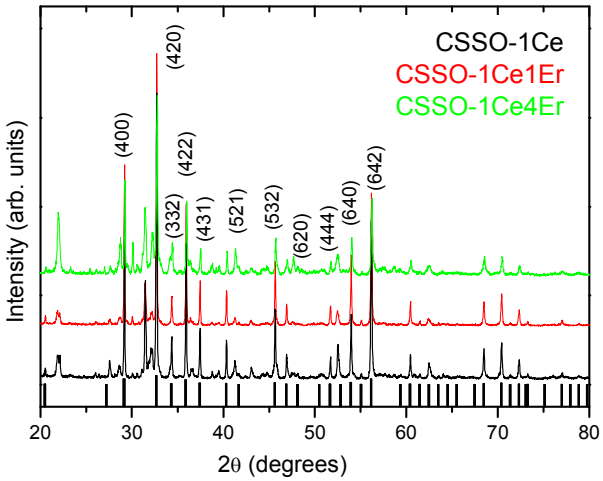

Fig.1. XRD patterns of undoped, Ce^{3+} and Ce^{3+}-Er^{3+} doped $Ca_3Sc_2Si_3O_{12}$ heat treated garnets; the main reflection planes are indicated. Standard peaks of $Ca_3Sc_2Si_3O_{12}$ (JCPDS file 72-1969) have been included for comparison purposes.

3. Results and discussion

Freeze-drying synthesis technique shows some advantages with reference to other precursor methods like co-precipitation or sol-gel method. The co-precipitation methods required that cations solubility in the reaction mixture be very low to achieve nominal composition, while in sol-gel method rests of carbon from the complexing agent or from the gelificant agent can remain, which not decompose until reached high temperatures. The amorphous product obtained using freeze-drying method only contains nitrates which decompose at low temperatures. This method has been successfully used in previous works obtaining pure phases and nanostructured materials at relatively low temperatures[16-18]. For all of these reasons, we have used the freeze-drying synthesis method for studying the influence of the doping concentration in the energy transfer processes of CSSO doped with Ce^{3+} and Er^{3+} ions.

3.1 Structural characterization

3.1.1. XRD phase characterization and crystal size. XRD patterns of Ce^{3+}-Er^{3+} doped garnets previously heat treated at 1200 ºC during 4 hours show a major phase, $Ca_3Sc_2Si_3O_{12}$, with secondary crystalline phase, like Ca_3SiO_5, Sc_2O_3 and SiO_2, see Fig. 1. These phases were also observed in our previous work about CSSO garnets codoped with Ce^{3+} and Tb^{3+} ions[19].Moreover, mean sizes of the nanocrystals have been obtained by using the Scherrer equation[20], from the full width at half maximum (FWHM) and the XRD peaks position.

$$d = \frac{k \cdot \lambda}{\beta \cdot \cos\theta} \quad (1)$$

where d is the crystal size, λ the X-ray wavelength, θ the diffraction angle, β the full-width at half maximum (FWHM) of the diffraction peak and K is a constant depending on particle shape (currently K = 0.9).The obtained nanocrystals mean sizes, shown in Table 2, are similar to those previously obtained by us in Ce^{3+}- Tb^{3+} codoped CSSO garnets[19].

CSSO-1Ce	110 nm
CSSO-1Ce1Er	138 nm
CSSO-1Ce4Er	88 nm

Table 2. Mean sizes of Ce^{3+}-xEr^{3+} (x= 0, 1 or 4) co-doped CSSO nanocrystals, in mol%, after thermal treatments at 1200 ºC for 4 hours.

Regarding the crystal structure of CSSO garnets, it corresponds to the cubic system with $Ia\bar{3}d$ space group (#230)[6]. The Ca^{2+} ions are situated in the center of eight-coordinated dodecahedra (24c), while Sc^{3+} ions are located in the center of six coordinated octahedra (16a) and Si^{4+} ions are in the center of four-coordinated tetrahedra (24d). It is known that in the $Ca_3Sc_2Si_3O_{12}$ garnet structure one dodecahedron is associated to four other dodecahedra and four octahedral; two tetrahedra by shared edges and other four octahedral by corner sharing[21]. According to the literature, Ca^{2+} ions (ionic radius 114 pm) are substituted for Ce^{3+} and Er^{3+} ions in the dodecahedral position and do not substitute Sc^{3+} ions because of the difference of the respective ionic radius, 75 pm for Sc^{3+} and up to 100 pm for Ce^{3+} (115 pm) and Er^{3+} (103 pm)[22-25].

3.1.2. Morphology. The morphology of the prepared doped powders calcined at 1200 ºC for 4 hours has been studied by SEM. Fig. 2 illustrates the irregularity in shape and size of the sintered material.

The mean size of the aggregated grains, around 40μm, is bigger than those obtained by other conventional synthesis process like sol-gel combustion or emulsion-evaporation methods, in which higher heat treatment temperatures are necessary to obtain aggregated grains around 1-10 μm[26,27]. On the other hand, it can be noted that the morphology of the samples seems to be affected by the Er^{3+} dopant concentration. When the Er^{3+} concentration increases from 0 to 1 mol%, an increment of the sinterization level could be observed. Further increases in the Er^{3+} concentration, from 2 to 4 mol%, does not result in a significant change of the sintering.

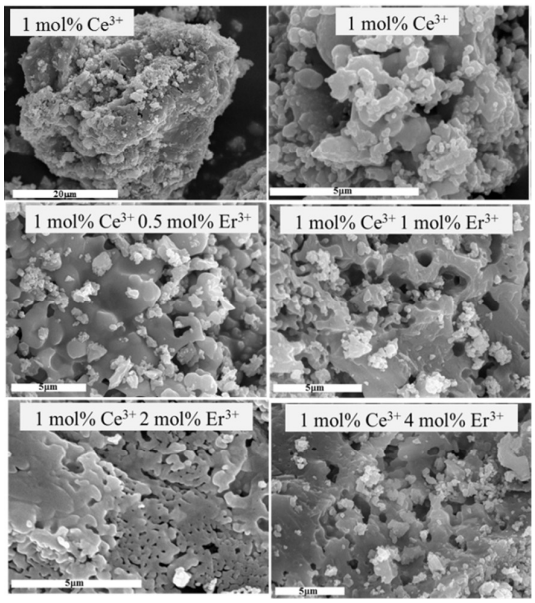

Fig. 2. SEM micrographs of $1Ce^{3+}$-xEr^{3+} (x = 0, 1, 2, 4), in mol%, co-doped $Ca_3Sc_2Si_3O_{12}$ garnets as a function of Er^{3+} ions concentration.

3.1.3. Relative concentration of Ce oxidation states (XPS). The garnets samples doped with high content of Ce (4 mol%), were also analyzed by X-ray photoelectron spectroscopy (XPS) to detect possible chemical changes in the surface of the samples. In particular, we used this technique in order to estimate the relative concentration of the two oxidation state of Ce (III and IV).

Figure 3 shows the high resolution XPS spectra of Ce 3d in the binding energy (BE) range 870-930 eV. The peaks between 870 and 895 eV belong to the Ce $3d_{5/2}$ levels while peaks between 895 and 913 eV correspond to the Ce $3d_{3/2}$ levels. The subscripts of U and V correspond to the oxidation state of Ce and the superscripts are an arbitrary label in order to differentiate the peaks of the same oxidation state.

The satellite peak at around 917 eV, which is not observed in the initial state of trivalent Ce, is a characteristic fingerprint of the presence of cerium (IV), indicating that there is a mixture of Ce(III) and Ce(IV) ions in the sample[28].

As it can been observed, the shape of Ce 3d spectral line is complex due to the overlapping of several doublet lines resulting from different final states of cerium after the emission of photoelectrons. Thus, it is well accepted the presence of Ce^{4+} ions lead to the appearance of three doublets and the Ce^{3+} ions produce two doublet in the XPS spectrum, with a total sum of ten lines. For the quantitative calculations of the Ce^{3+} and the Ce^{4+} concentrations, the high resolution XPS spectra of Ce 3d were deconvoluted in ten lines (see Fig. 3), according to the oxides of $Ce(III)_2O_3$ and $Ce(IV)O_2$[29]. In this work, U and V notations are used for the assignment of Ce 3d corresponding to $3d_{3/2}$ and $3d_{5/2}$, respectively.

In the Ce^{3+} species, $V^1_{3+} - U^1_{3+}$ are the shakes down peaks and $V^2_{3+} - U^2_{3+}$ are the main peaks. In the Ce^{4+}, two shake down peaks $V^1_{4+} - U^1_{4+}$ and $V^2_{4+} - U^2_{4+}$ were assigned, and the main peaks $V^3_{4+} - U^3_{4+}$ were the characteristic peaks of Ce^{4+}.

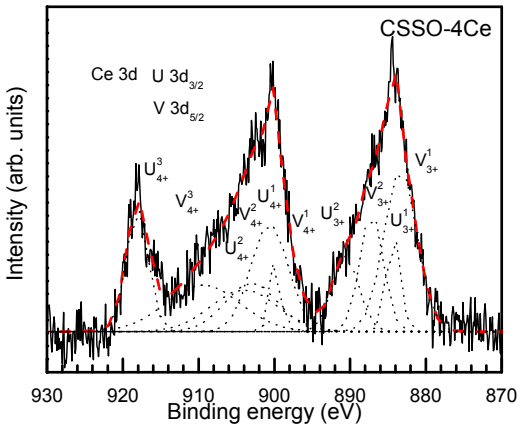

Fig. 3. High resolution XPS spectra of Ce 3d region (solid line) in CSSO-4Ce garnet. Deconvolution of the peaks is indicated in dotted lines. Red dash line represents the best fit obtained taking into account all deconvolutions.

The concentration of Ce^{3+} and Ce^{4+} can be determined from the ratio of the integrated peak areas according to the following equations[30].

$$Ce^{3+} = V^1_{3+} + V^2_{3+} + U^1_{3+} + U^2_{3+}$$

$$Ce^{4+} = V^1_{4+} + V^2_{4+} + V^3_{4+} + U^1_{4+} + U^2_{4+} + U^3_{4+}$$

$$\left[Ce^{3+}\right] = \frac{Ce^{3+}}{Ce^{3+} + Ce^{4+}} = \frac{V^1_{3+} + V^2_{3+} + U^1_{3+} + U^2_{3+}}{V^1_{3+} + V^2_{3+} + U^1_{3+} + U^2_{3+} + V^1_{4+} + V^2_{4+} + V^3_{4+} + U^1_{4+} + U^2_{4+} + U^3_{4+}} \quad (2)$$

where the notations Ce(III) and Ce(IV) represent the corresponding sums of the integrated peak areas related to the Ce XPS spectrum. By applying this equation, we obtained rates of about 40 and 60% for Ce^{3+} and Ce^{4+}, respectively.

It would be remarked that XPS is a surface technique which explores the materials until a depth of about 10 nm. However, when this technique is used, as in our case, with crystal sizes about 100 nm, the analysed volume corresponds to about the half of the total volume of the nanocrystals. Therefore, the XPS results indicate that a large fraction of the cerium ions are present in our sample as Ce^{3+} and then participate in the luminescent processes.

3.1.4. Laser Raman spectra. Raman experiments of undoped and Ce^{3+} doped CSSO garnets were carried out in order to complete the structural characterization. Fig. 4 shows the Raman spectra of these garnets excited at 632.8 nm. These spectra were measured at different areas of the garnets in order to confirm the homogeneity of the samples. The spectra mainly present the usual features of $Ca_3Sc_2Si_3O_{12}$ garnets, together with a peak of the Sc_2O_3 phase[30] at 420 cm^{-1}.

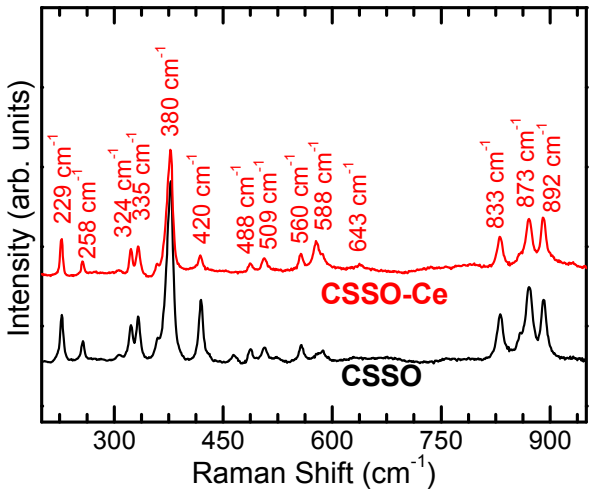

Fig. 4. Raman spectra of CSSO and CSSO-Ce obtained under 632.8 nm laser excitation.

According to previous studies, $Ca_3Sc_2Si_3O_{12}$ garnets have 25 Raman active vibration modes expected on the basis of the analysis of the cubic space group Ia $3\bar{d}$ of the silicate garnets[21,31–35]. In particular, 13 of them are observed in the region of 200–950 cm^{-1} as can be observed in Fig. 4, together with the peak at 420 cm^{-1} corresponding to the mode Fg of Sc_2O_3 phase[30]. According to these studies, the band assignments can be summarized as follows.

The high frequency modes (800–950 cm^{-1}) are related to symmetric and asymmetric internal stretching vibrations of rigid SiO_4 tetrahedra. The modes lying from 450 to 700 cm^{-1} are assigned to bending motions of these tetrahedra. Finally, the remaining lattice modes (200–415 cm^{-1}) involve rotations and translations of the SiO_4 groups, octahedrally coordinated trivalent cations and dodecahedrally coordinated divalent cations. On the other hand, in a previous work we demonstrate that the intensity reduction of the peak corresponding to the Sc_2O_3 phase when doping with RE^{3+} ions is in agreement with the XRD results. Moreover, this Sc_2O_3 phase almost vanishes by RE^{3+} doping[19].

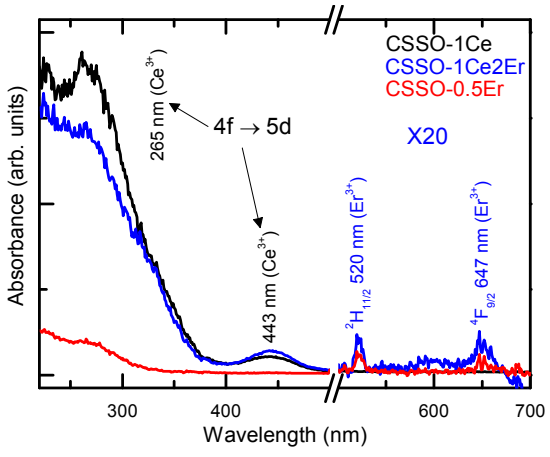

Fig. 5. Absorption spectra of Ce^{3+} and Er^{3+} doped and Ce^{3+}-Er^{3+} codoped CSSO garnets. Spectra are multiplied by a factor of 20 in the range 500-700 nm.

3.2. Spectroscopic analysis

3.2.1. Absorption Spectra. Absorption spectra of Ce^{3+} and Er^{3+} doped and Ce^{3+}- Er^{3+} codoped CSSO garnets are shown in Fig. 5. A strong absorption peak is observed at 265 nm together with another peak at 440 nm, which correspond to 4f → 5d transitions of Ce^{3+} ions. On the other hand, weaker Er^{3+} absorption peaks are also observed at 520 and 647 nm, corresponding to intraconfigurational 4f-4f transitions in the visible range to the $^2H_{11/2}$ and $^4F_{9/2}$ levels of Er^{3+} ions, respectively. As result, it is found that Ce^{3+} ions are more efficiently excited than Er^{3+} ion in the UV-blue spectral range.

3.2.2. Luminescence

3.2.2.1. Ce^{3+} and Er^{3+} single doped garnets. The photoluminescence spectra of Ce^{3+} and Er^{3+} 1 mol% single-doped CSSO garnets are shown in Fig. 6. The excitation and emission spectra corresponding to 1 mol% Ce^{3+} doped garnets are similar to those obtained by the authors in a previous work[19]. Moreover, these spectra are also similar to those obtained by Cheng et al[33] for Ce^{3+} ions in a close matrix. The emission spectrum shows a broad emission band with two components, at 505 and 550 nm. The component at 505 nm corresponds to the interconfigurational transition of the Ce^{3+} ions from the lowest energy 5d level to the ground level, i.e. $^5D_{3/2}$→$^2F_{5/2}$, shown in Fig. 6. The component located at 550 nm corresponds to the transition from the same emitting level to the first excited 4f level, i.e. $^5D_{3/2}$→$^2F_{7/2}$. Moreover, the excitation spectrum of these emissions presents two peaks, at 311 and 450 nm. The peak at 450 nm is two orders of magnitude more intense.

On the other hand, in the samples single-doped with Er^{3+} under excitation at 378 nm, that corresponds to the $^4I_{15/2}$ → $^4G_{11/2}$ transition of Er^{3+} ions, emissions at 545, 560, 660 and 850 nm are observed, see Fig. 6. These emissions correspond to transitions from the $^2H_{11/2}$, $^4S_{3/2}$, $^4F_{9/2}$ and $^4I_{9/2}$ levels to the ground state $^4I_{15/2}$, respectively. These peaks, with well resolved Stark components, are typical of ions in crystalline environments and they are indicative of the effective incorporation of the Er^{3+} ions into the CSSO garnets.

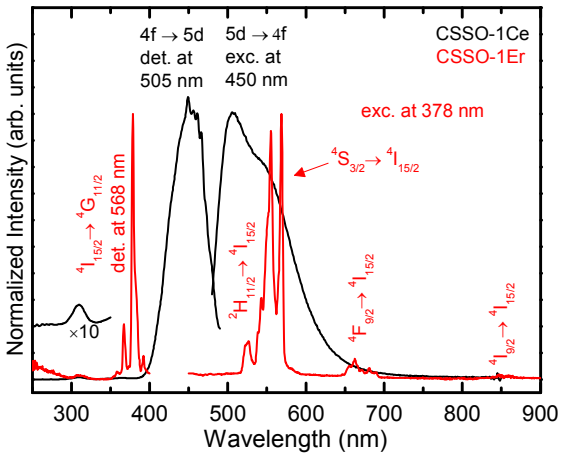

Fig. 6. Normalized excitation and emission spectra of Ce^{3+} (black) and Er^{3+} (red) 1 mol% single-doped CSSO garnet with Ce^{3+} and Er^{3+}, respectively.

3.2.2.2. Ce^{3+}- Er^{3+} codoped garnets. The incorporation of Er^{3+} ions into Ce^{3+}-Er^{3+} codoped CSSO garnets results in decreasing of the Ce^{3+} emission intensity obtained under direct excitation of these ions, see Fig. 7. An excitation wavelength of 425 nm was selected in order to excite Ce^{3+} ions without simultaneous excitation of Er^{3+} ions. However, VIS and NIR luminescence of Er^{3+} ions at 540, 850 and 1550 nm is also observed, being the 1550 nm emission much more intense than the others, as it is shown in Fig. 7. It would be noticed that the highest emission intensity at 1550 nm is obtained for the Er^{3+} intermediate concentration of 1.0 mol%.

These Er^{3+} emissions are due to energy transfer from Ce^{3+} to Er^{3+} ions. These energy transfer processes are caused by the overlap of the broad Ce^{3+} emission at 505-550 nm, see Fig. 6, with the Er^{3+} absorption, mainly at 520 nm ($^4I_{15/2} \rightarrow {}^2H_{11/2}$), see Fig. 5.

On the other hand, the decrease of the Ce^{3+} emission with the increase of the Er^{3+} concentration is not followed by an equivalent enhancement of the NIR emission of these ions, as observed in Fig. 7. For this reason, the excited state dynamics after pulsed excitation was studied in order to analyse the mechanisms involved in the luminescence of these materials.

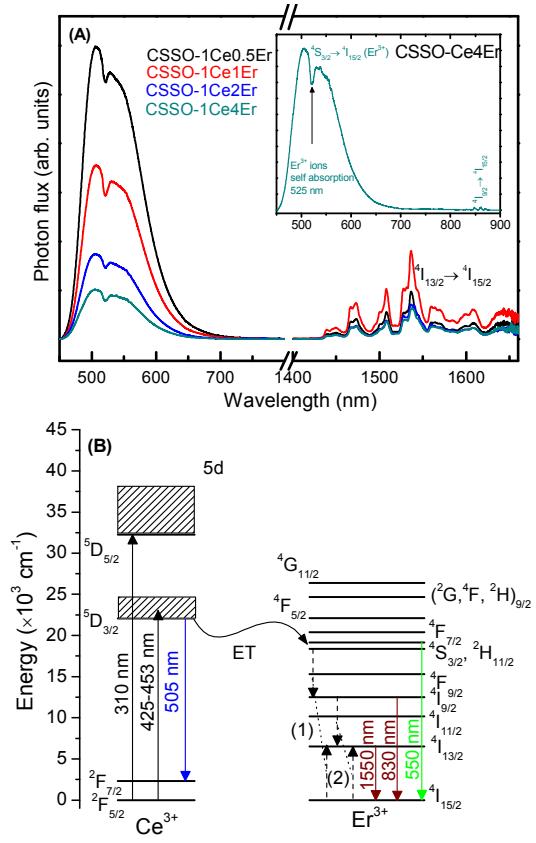

Fig. 7. (A) VIS-NIR emission spectra of Ce^{3+}-Er^{3+} codoped CSSO garnets under excitation at 425 nm. Inset shows a magnified VIS spectrum of $1Ce^{3+}$-$4Er^{3+}$ codoped CSSO garnet. (B) Energy level diagrams of Ce^{3+} and Er^{3+} ions with main excitation and emission transitions, indicated by solid arrows, and energy transfer mechanisms, indicated by dash arrows.

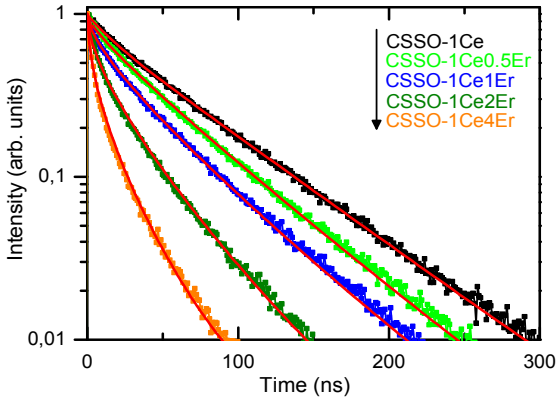

Fig. 8. Decays of Ce^{3+} doped and Ce^{3+}-Er^{3+} codoped CSSO garnets with excitation at 405 nm and detection at 505 nm. The red lines represent the best fits of the experimental results to Equation 3.

3.2.3. Excited State Dynamics. The decays of the Ce^{3+} emission in Ce^{3+}-xEr^{3+} codoped CSSO garnets (x = 0, 0.5, 1, 2 and 4 mol%), obtained after excitation and detection at 405 and 505 nm, respectively, are shown in Fig. 8. These decays present non-exponential behaviour related to the energy transfer from Ce^{3+} to Er^{3+} ions after Ce^{3+} excitation. These results can be analysed by using the Inokuti-Hirayama expression for dipole-dipole interaction between donors and acceptors[36].

$$I(t) = I(0) \cdot exp\left[-\frac{t}{\tau} - Q\left(\frac{t}{\tau}\right)^{1/2}\right] \quad (3)$$

where τ is the intrinsic lifetime of the donors and Q is a parameter related to the energy transfer probability, which can be calculated from the fits. Good fits are obtained, as shown in Fig. 8, with values for Q increasing from 0.48 to 2.92 when the Er^{3+} concentration increases from 0.5 to 4 mol%.

On the other hand, the energy transfer efficiency from Ce^{3+} to Er^{3+} ions, η_{ET}, can be calculated by using Equation 4,

$$\eta_{ET} = 1 - \frac{\tau_{Ce-xEr}}{\tau_{Ce-0Er}} \quad (4)$$

where τ_{Ce-0Er} and τ_{Ce-xEr} are the effective lifetime of Ce^{3+} emission in single and codoped samples, respectively, calculated from the decays shown in Fig. 8. The obtained results are shown in Table 3, for the different garnets. As it can be see, the lifetime of Ce^{3+} ion gradually decreases with the Er^{3+} concentration while the energy transfer efficiency increases up to 0.82 for the highest Er^{3+} doping level of 4 mol%. The increase of this energy transfer efficiency from Ce^{3+} ions with the Er^{3+} concentration is roughly in agreement with the decrease of the Ce^{3+} emission, shown in Fig. 7, when the Er^{3+} concentration increases. A similar effect was observed by G. Zhang et al.[37] in case of Ce^{3+}-Pr^{3+} codoped $CaLaGa_3S_6O$ garnets. However, the NIR Er^{3+} emission initially increases with the concentration of these ions but it decreases for concentrations over 1 mol%, see Fig. 7.

Samples	$\tau_{Ce\text{-}xEr}$ (ns)	η_{ET}	τ_{xEr} (ms)	$\eta_{Er\text{-}emis}$	$\frac{I_{Er}}{I_{Ce}}$	
					Calc.	Exp.
CSSO-1Ce	56.0	-	-	-		
CSSO-1Ce0.5Er	44.5	0.21	6.0	1.0	0.27	0.10
CSSO-1Ce1Er	33.6	0.40	5.9	0.98	0.65	0.32
CSSO-1Ce2Er	19.8	0.65	1.6	0.27	0.50	0.28
CSSO-1Ce4Er	10.0	0.82	0.9	0.15	0.68	0.45

Table 3. Effective lifetime of Ce^{3+} emission, $\tau_{Ce\text{-}xEr}$. Energy transfer efficiency η_{ET}, obtained by means of Eq. 3. Effective lifetime of the Er^{3+} NIR emission, τ_{xEr}. Quantum efficiency of the Er^{3+} NIR emission $\eta_{Er\text{-}emis}$. Calculated and experimental values for the emissions ratio I_{Er}/I_{Ce}.

Having such hints, we measured the decay of the NIR Er^{3+} emission at 1550 nm after pulsed excitation at 405 nm, corresponding to direct excitation of Er^{3+} ions. These decays, shown in Fig. 9, present a single exponential behaviour for the lowest Er^{3+} concentrations of 0.5 and 1 mol%, with a lifetime of 6.0 ms. Meanwhile, for concentrations above 1 mol% the emission decays are quite faster, with effective lifetimes presented in Table 3. This behaviour would be due to quenching of the emission by energy migration until luminescence traps.

From these effective lifetimes, we obtained the quantum efficiency of the NIR Er^{3+} emission by using Equation 5

$$\eta_{Er-emis} = \frac{\tau_{xEr}}{\tau_{0.5Er}} \quad (5)$$

where τ_{xEr} and $\tau_{0.5Er}$ are the effective lifetime for the different Er^{3+} concentrations. The results obtained for the quantum efficiency of this emission, given in Table 3, present large values, close to 1, for Er^{3+} concentration up to 1 mol% with an important decrease for larger concentrations.

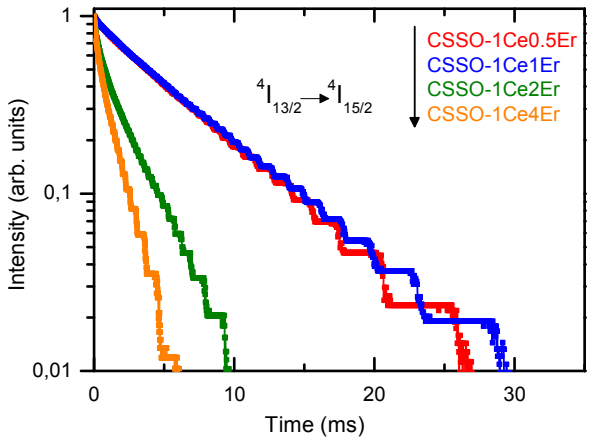

Fig. 9. Decays of Ce^{3+}-Er^{3+}codoped CSSO garnets excited at 405 nm and detected at 1550 nm, corresponding to $^4I_{13/2} \rightarrow {}^4I_{15/2}$ transition

Now we can calculate the expected ratio of Er^{3+} to Ce^{3+} integrated emissions, taking into account the energy transfer efficiency from the Ce^{3+} ions and the quantum efficiency of the NIR Er^{3+} emission, by using Equation 6.

$$\frac{I_{Er}}{I_{Ce}} = \frac{\eta_{ET} \cdot \eta_{Er-emis}}{\eta_{ET} - 1} \quad (6)$$

The obtained results are shown in Table 3 and would be compared with the experimental values obtained directly from the integrated photon fluxes of Er^{3+} and Ce^{3+} emissions, from spectra in Fig. 7.

The experimental emission ratios obtained experimentally from spectra in Fig. 7 are lower than the values calculated by using Eq. 5. This indicates that in Ce^{3+}-Er^{3+} co-doped garnets the energy transfer from Ce^{3+} to Er^{3+} is not the only mechanism involved in the reduction of the Ce^{3+} emission. A similar result was obtained in garnets codoped with Ce^{3+} and Tb^{3+} ions[19]. But in this case we obtain a relatively high efficiency in the transfer from Ce^{3+} ions to the acceptor ions. For the optimum composition of 1 mol% of Er^{3+}, following Fig.6, about half of the non-radiative decays of Ce^{3+} ions take to NIR emission of Er^{3+} ions (from the comparison of experimental and calculated ratios I_{Er}/I_{Ce} in Table 3).

Conclusions

$Ca_3Sc_2Si_3O_{12}$ garnets doped with Ce^{3+} and Er^{3+} ions have been successfully synthesized by a freeze-drying precursor method. After heat treatment at 1200 ºC $Ca_3Sc_2Si_3O_{12}$ nanocristals, with a mean size about 100 nm have been obtained. From XPS measurements we obtained that a large fraction of the cerium ions are present as Ce^{3+} ions in these garnets. Moreover, luminescence features indicated that Ce^{3+} and Er^{3+} dopant ions are effectively incorporated into the garnets. In addition, codoping with Ce^{3+}-Er^{3+} ions results in energy transfer processes from Ce^{3+} to Er^{3+} ions, allowing to obtain efficiently NIR emission at 1.5 µm under blue excitation. The efficiency of these non-radiative energy transfer process has been analyzed by means of excited state dynamics as a function of the doping concentration. From these results we found that NIR luminescence of the garnets is maxima for CSSO-C1E. For higher Er^{3+} concentration the energy transfer efficiency increases, up to 82% for 4 mol% of Er^{3+}, but also an appreciable increase of quenching effects is observed for Er^{3+} concentration over 1 mol%.

Acknowledgements

The authors would like to thank Ministerio de Economía y Competitividad (MAT2013-42407-R cofunded by FEDER funds) and Fundación CajaCanarias (Proyecto HIDROSOLAR, ENER02) for financial support. J.J. Velázquez also thanks to Ministerio de Economía y Competitividad for Posdoctoral grant (FPDI-2013-16895). Fernando Rivera-López thanks to Cajasiete for financial support related with Servicio de Sistema Multitécnicas de Análisis

de Superficies (SEGAI-ULL). We also thanks to group MATMOL, from University of La Laguna (ULL), for the possibility of use the UV-Visible absorbance spectrophotometer. This research was partially performed in the framework of the projects CNR-PAS (2014-2016) and COST ACTION MP1401. R.R. Gonçalves and M. Ferrari acknowledge Brazilian Scientific Mobility Program "Ciências sem Fronteiras".

References

1. B. M. van der Ende, L. Aarts and A. Meijerink, Phys. Chem. Chem. Phys., 2009, 11, 11081. DOI: 10.1039/B913877C.

2. J. Zhou, Y. Teng, X. Liu, S. Ye, Z. Ma and J. Qiu , Phys. Chem. Chem. Phys., 2010, 12, 13759. DOI: 10.1039/C0CP00204F

3. F. Piccinelli, A. Speghini, G. Mariotto, L. Bovo, M. Bettinelli, J. of Rare Earths, 2009, 27, 555. DOI:10.1016/S1002-0721(08)60287-2.

4. D.Q. Chen, Y.S. Wang, Y.L. Yu, P. Huamg and F.Y. Weng, J. Appl. Phys. 2008, 104, 116105. DOI: 10.1063/1.3040005.

5. P. Dorenbos, J. Lumin., 2000, 91, 106. DOI:10.1016/S0022-2313(00)00197-6.

6. J. Ueda and S. Tanabe, J. Appl. Phys, 2009, 106, 043101. DOI: 10.1063/1.3194310.

7. X. Chen, J. Wu, X. Xu, Y. Zhang, N. Sawanobori, C. Zhang, Q. Pan, and G. J. Salamo, Opt. Lett. ,2009, 34, 887. DOI: 10.1364/OL.34.000887

8. Y. Suzuki, M. Kakihana, Y. Shimomura and N. Kijima, J Jpn Soc Powder Powder Metall 2007, 54, 44. DOI: 10.2497/jjspm.54.44

9. Y. Shimomura, T. Honma, M. Shigeiwa, T. Akai, K. Okamoto and N. Kijima, J. Electrochem. Soc., 2007, 154, 35 DOI: 10.1149/1.2388856.

10. K.V Ivanovskikh., A. Meijerink, F. Piccinelli, A. Speghini, E.I. Zinin, C. Ronda and M. Bettinelli, J. Lumin. 2010, 130, 893. DOI: 10.1016/j.jlumin.2009.12.031.

11. M. Bettinelli, A. Speghini, F. Piccinelli, A.N.C. Neto, O.L. Malta, J. Lum., 2011, 131, 1026. DOI: 10.1016/j.jlumin.2011.01.016.

12. C. Feng, Y. Meng, X. Liu, J. Wang and L. Yang, Xiyou Jinshu/ Chin. J. Rare Met. DOI: 10.3969/j.issn.0258-7076.2013.01.016

13. Y. Chen, J, Feng, Y. Pan, J. Li, S. Zeng, M. Liang, Z. Liu, N. Li, Y. Su, J. Lum., 2014, 148, 153. DOI:10.1016/j.jlumin.2013.12.015

14. J. Qiao, J. Zhang, X. Zhang, Z. Hao, Y. Liu and Y. Luo, Dalton Trans., 2014, 43, 4164. DOI: 10.1039/C3DT52902A,.

15. W. Wan, Q. Xiao, C. Yang, K. Meng, Kuei Suan Jen Hsueh Pao/Journal of the Chinese Ceramic Society, Volume 38, Issue 10, October 2010, 38, 1862. Pages 1862-1866.

16. M.O. Mazan, J. Marrero-Jerez, A. Soldati, P. Núñez, S. Larrondo, Int J. Hydrogen Energ, 2015, 40, 3981. DOI: 10.1016/j.ijhydene.2015.01.006

17. M. Amsif, D. Marrero-López, A. Magrasó, J. Peña-Martínez, J.C Ruiz-Morales and P. Núñez, J. Eur Ceram Soc, 2009, 29, 131 DOI: 10.1016/j.jeurceramsoc.2008.06.001

18. J. Marrero-Jerez, S. Larrondo, E. Rodríguez-Castellón and P. Núñez, Ceram. Int., 2014, 40, 6807 DOI: 10.1016/j.ceramint.2013.11.143.

19. J .J. Velázquez, R. Fernández-González, J. Marrero-Jerez, V. D. Rodríguez, A. Lukowiak, A. Chiappini, A. Chiasera , M. Ferrari and P. Núñez, Opt. Mat, 2015, 46, 109 DOI: 10.1016/j.optmat.2015.03.057.

20. B.D. Cullity, Elements of X-ray Diffraction (Addison-Wesley, Massachusetts, 1978).

21. W. Yun-Fang, C. Ya-Han, N. Yung-Tang and C. In-Gann, J. Am. Ceram. Soc., 2013, 96, 234 DOI: 10.1111/jace.12034

22. Y. Liu, X. Zhang, Z. Hao, Y. Luo, X. Wang, J. Zhang. J. Mater. Chem., 2011, 21, 16379. **Falta DOI**

23. M.S. Kishore, N.P. Kumar, R.G. Chandran, A.A. Setlur, Electrochem. and Solid-State Lett. 2010, 13(6), J77-J80. **Falta DOI**

24. R.G. Burns. Ionic radii of transition metals and related cations. In: Mineralogical Applications of Crystal Field Theory. 1993, 464-465. Cambridge Topics in Mineral Physics and Chemistry. (Nº5). 2nd ed. Cambridge: Cambridge University Press. DOI: 10.1017/CBO9780511524899.016

25. V. Zepf, Rare Earth Elements. A New Approach to the Nexus of Supply, Demand and Use: Exemplified along the Use of Neodymium in Permanent Magnets. Springer Theses. ISBN 978-3-642-35458-8.

26. Y. Liu, J. Hao, W. Zhuang and Y. Hu, J. Phys. D: Appl. Phys., 2009, 42, 245102. DOI: :10.1088/0022-3727/42/24/245102

27. N. Enomoto, T. Sakai, M. Inada, Y. Tanaka and J. Hojo, J. Cer. Soc. Japan, 2010, 118, 1067. DOI:10.2109/jcersj2.118.1067

28. E. Bêche, P. Charvin, D. Perarnau, S. Abanades, and G. Flamant, Surf. Interface Anal., 2008, 40, 264. DOI: 10.1002/sia.2686

29. S. Gavarini, M.J. Guittet, P. Trocellier, M. Gauthier-Soyer, F. Carrot and G. Matzen, J. Nucl. Mater., 2003, 322, 111. DOI: 10.1016/S0022-3115(03)00306-4

30. J. Zhang, X. Ju, Z.Y. Wu, T. Liu, T.D. Hu, Y.N. Xie and Z.L. Zhang, Chem. Mater., 2001, 13, 4192. DOI: 10.1021/cm010235p.

31. N.D. Todorov, M.V. Abrashev, V. Marinova, M. Kadiyski, L. Dimowa, and E. Faulques Phys. Rev. B 2013¸87, 104301.

32. Ubaldini A and Carnasciali M M, J. Alloys Compd. 2008, 454, 374.

33. Y. Cheng, K. Cheah, M. Gong, J. of Lum. 2011, 131, 1589.

34. A.M. Hofmeister and A. Chopelas, Phys. Chem. Minerals 1991, 17, 503.

35. S.P. Feofilov, D.V. Arsentyev, A.B. Kulinkin, R.I. Zakharchenya, J. of Lum. 2011, 131, 438.

36. M. Inokuti and F. Hirayama, J. Chem. Phys. 1965, 43, 1978. DOI: 10.1063/1.1697063.

37. G. Zhang, C. Liu, J. Wang, X. Kuang and Q. Su, J. Mater. Chem., 2012, 22, 2226, DOI: 10.1039/c1jm14942c